COMMUNICATION

Hierarchical zigzag $Na_{1.25}V_3O_8$ nanowires with topotactically encoded superior performance for sodium-ion battery cathodes†

Yifan Dong,‡[a] Shuo Li,‡[ab] Kangning Zhao,[a] Chunhua Han,[a] Wei Chen,*[a] Bingliang Wang,[a] Lei Wang,[a] Boan Xu,[a] Qiulong Wei,[a] Lei Zhang,[a] Xu Xu[ac] and Liqiang Mai*[a]

We report a facile method to topotactically synthesize $Na_{1.25}V_3O_8$ nanowires with a novel hierarchical zigzag structure. The unique morphology can provide an increased electrode−electrolyte contact area and better strain accommodation; also the topotactic intercalation method can improve structure integrity and robustness. The as-synthesized material delivers a capacity of 172.5 mA h g^{-1} at 100 mA g^{-1}, shows excellent cyclability with a capacity fading of only 0.0138% per cycle at 1 A g^{-1} for 1000 cycles, and high rate capability as a sodium-ion battery cathode. We propose that the novel morphology as well as intrinsically advantageous structural features can synergistically facilitate the kinetics and stability, resulting in superior electrochemical performance.

With the increasing demand for portable electronic devices, electrical vehicles and energy grid, the development of energy storage systems with high power, good stability and safety, as well as high efficiency and low cost is a critical need.[1–7] Lithium-ion batteries play the dominant role in energy storage currently because of their highest energy density among practical rechargeable batteries. However, the high cost and the insufficient lithium resources will limit the application of lithium-ion batteries in future, especially in large-scale energy storage systems. Therefore, the search for an alternative to lithium-ion batteries is significant and required.[8–12] Sodium is located just below lithium in the periodic table and shares many similarities with lithium in many aspects. Due to the lower cost, improved safety characteristics and similar intercalation chemistry compared to lithium-based batteries, sodium-ion batteries

[a] State Key Laboratory of Advanced Technology for Materials Synthesis and Processing, Wuhan University of Technology, Wuhan 430070, China. E-mail: mlq518@whut.edu.cn; chenwei2005@whut.edu.cn

[b] Department of Chemistry, University of Wisconsin–Madison, 1101 University Avenue, Madison, Wisconsin 53706, USA

[c] Department of Chemistry and Biochemistry, University of California, Los Angeles, California 90095, USA

‡ These authors contributed equally to this work.

Broader context

Sodium-ion batteries have been paid significant attention as an immediate alternative to lithium-ion batteries because of their prospective sustainability and cost-effectiveness. To satisfy their practical use, sodium-ion battery electrodes should possess long lifespan, good rate capability and high energy density. However, the intrinsic limitations of sodium-ion batteries challenge their practical use, such as lower voltage, smaller diffusion coefficient and more significant impact on the electrode crystal structure during battery operation compared with lithium-ion battery counterparts. To overcome these limitations, careful design and optimization of the electrode materials is necessary. Here we successfully synthesized hierarchical zigzag structured $Na_{1.25}V_3O_8$ nanowires *via* a facile topotactic intercalation method. The as-synthesized $Na_{1.25}V_3O_8$ nanowires exhibit excellent stability, rate capability and high capacity as sodium-ion battery cathodes, which is very promising for their application in sodium-ion batteries. The improved performance is due to: (1) the unique morphology, which can provide increased electrode–electrolyte contact area and better strain accommodation; and (2) the topotactic intercalation method, which improves the structure integrity and robustness. The concept that novel morphology and advantageous structure features can synergistically optimize the material performance significantly is instructive for designing new materials for the energy field.

become the immediate and promising candidate for replacement of lithium-ion batteries in the foreseeable future.[13–16] Nevertheless, the intrinsic limitations of sodium-ion batteries challenge the practical use, like the lower voltage, smaller diffusion coefficient and more significant impact on the electrode crystal structure during Na ion intercalation/deintercalation.[17–19] It is imperative to find suitable sodium-ion battery electrodes with high capacity, long lifespan and satisfying rate performance.

Similar to $Li_{1+x}V_3O_8$, which is an ideal material for lithium-ion batteries and has been studied extensively, $Na_{1+x}V_3O_8$ is considered to be a promising cathode material because of its high-specific capacity due to the multiple oxidation states, good structural stability, low cost and safety features. The $Na_{1+x}V_3O_8$ crystal structure is a layered structure composed of V_3O_8 polyhedra layers, and the Na ions are located between the layers in the octahedral sites predominantly. The Na ions situated at the

This journal is © The Royal Society of Chemistry 2015

Energy Environ. Sci., 2015, **8**, 1267–1275 | **1267**

octahedral sites act as pillar cations to stabilize the structure, making this configuration very advantageous. During the charge–discharge process, this stabilized structure can be maintained and better cyclability can be achieved.[20–22] Besides, as Na ions have a larger radius than lithium ions, the interlayer distance of $Na_{1+x}V_3O_8$ is larger than that of $Li_{1+x}V_3O_8$, which results in the higher capacity and better ionic mobility in $Na_{1+x}V_3O_8$. It is reported that $Na_{1+x}V_3O_8$ has better lithium storage capability than its isostructure $Li_{1+x}V_3O_8$.[23–26]

However, there are limited reports on $Na_{1+x}V_3O_8$ used as sodium-ion battery electrodes, and the performances are not satisfactory to meet the standards of practical application.[20,22,27] To become a good candidate electrode for rechargeable batteries, an electrode material should possess a suitable intrinsic crystal structure which can provide good ion transport pathways and avoid structural degradation during cycling effectively. And the morphology of the material should be carefully designed to facilitate efficient electrochemical reactions, to improve morphology integrity and robustness as well as to avoid self-aggregation during cycling.[28–33] Herein, we proposed a facile route to synthesize hierarchical $Na_{1.25}V_3O_8$ (NVO) nanowires with a zigzag shape *via* a facile topotactic intercalation method. The topotactic intercalation can improve the crystal structure robustness effectively without damaging the morphology.[34] Concurrently, by using a suitable additive CTAB, we are able to fabricate the hierarchical zigzag $Na_{1.25}V_3O_8$ nanowires with good uniformity. The hierarchical zigzag nanowire structure can shorten Na ion diffusion pathways, increase electrode–electrolyte contact area, and provide better strain accommodation and morphology integrity to eliminate the degradation and self-aggregation. During Na ion intercalation/deintercalation, the structural degradation and self-aggregation can be significantly alleviated (Fig. 1). With the synergistic effect of the suitable structure and morphology, our as-synthesized hierarchical $Na_{1.25}V_3O_8$ nanowires exhibit unprecedentedly excellent capacity and rate capability when investigated as a cathode material in sodium-ion batteries.
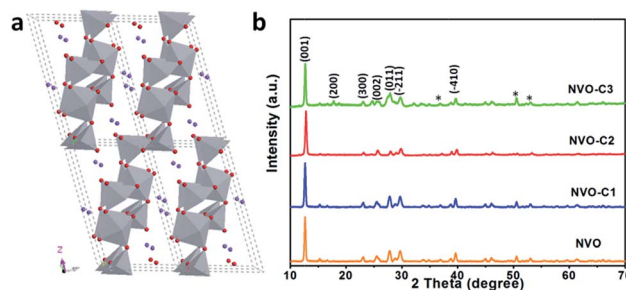
Fig. 2 Illustration of NVO crystal structure (a) and XRD patterns of simple NVO, NVO-C1, NVO-C2 and NVO-C3 (b).

Results

The NVO crystal structure is generally composed of layers of V_3O_8 polyhedra, as shown in Fig. 2a. The chains of VO_6 octahedra and those of VO_5 pyramids extending along the axis are linked by corner-shared oxygen atoms to form a continuous V_3O_8 framework. The Na ions are located predominantly in the octahedral sites with a full occupancy and the excess Na ions are located in the tetrahedral sites with some probability. During discharge, the Na ions can be accommodated in the sites between the layers, providing high theoretical capacity. Fig. 2b shows the X-ray diffraction (XRD) patterns of the NVO hierarchical nanowires with different CTAB amounts used during the synthesis. The samples are labelled as NVO-C1, NVO-C2, NVO-C3 and simple NVO nanowires for the 0.05, 0.1, 0.2 g and no CTAB amount in the synthesis. It can be seen that all the characteristic peaks for each sample are identical, indicating that the addition of CTAB has no influence on the phase structure of NVO. All the diffraction peaks of the patterns with different CTAB amounts can be readily indexed to a monoclinic phase of $Na_{1.25}V_3O_8$ (JCPDS no. 24-1156). There are a few weak peaks from $Na_{1.1}V_3O_{7.9}$ (JCPDS no. 45-0498) marked with asterisks, which should be attributed to the deficiencies during calcination.[24]
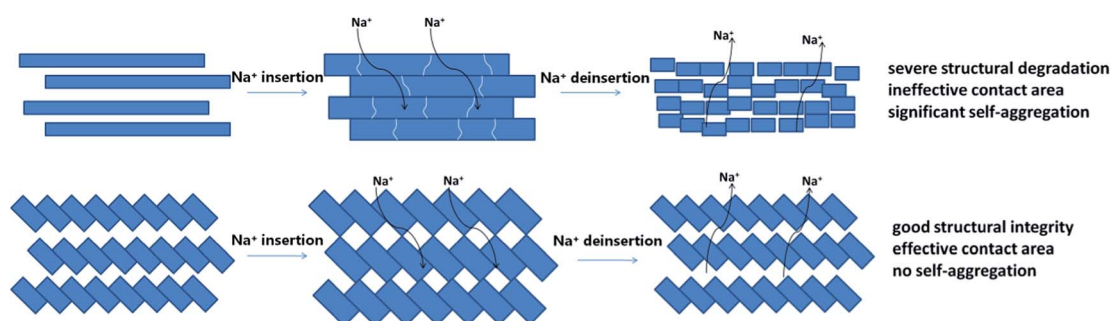
Fig. 1 Schematic illustration of the electrochemical process for the non-topotactically synthesized simple nanowire structure and topotactically synthesized hierarchical zigzag nanowire structure of $Na_{1.25}V_3O_8$. In the non-topotactically synthesized simple nanowire structure (upper), the crystal structure is not stable and the strain could not completely and promptly release, and the nanowires tend to aggregate and the structure is damaged during cycles, leading to poor cycling performance. The topotactically synthesized hierarchical zigzag nanowire structure (lower) provides good structural integrity, facile strain relaxation for swelling during cycling as well as effective electrode–electrolyte contact area.

The hierarchical zigzag NVO nanostructures were fabricated by using as-synthesized $H_2V_3O_8$ nanowires as the precursor and template. The XRD pattern of $H_2V_3O_8$ can be indexed to a pure orthorhombic phase (JCPDS no. 85-2401) as shown in Fig. S1a.†[35] The $H_2V_3O_8$ has a uniform nanowire morphology with a diameter of 100–200 nm and the surface is very smooth, as shown in the field-emission scanning electron microscopy (FESEM) image in Fig. S1b.† The morphologies of the NVO nanowires with different CTAB amounts during synthesis are shown in the FESEM images in Fig. S2a–d,† respectively. Without CTAB addition, the morphology of simple NVO is a typical nanowire structure, with a diameter around 200 nm and smooth surface (Fig. S2a†). This is in good correspondence with the morphology of the $H_2V_3O_8$ nanowire precursor. For the morphology of NVO-C1 (Fig. S2b†), the nanowire structure is maintained, but the surface becomes much rougher compared to the $H_2V_3O_8$ nanowire precursor morphology. The NVO-C2 has a 1D nanowire structure which is composed of many short nanorods and voids in between intermittently, exhibiting a hierarchical nanowire structure (Fig. S2c†). For NVO-C3, it can be seen that the nanowires are composed of short nanorods similar to NVO-C2, but no significant voids in the structure are observed (Fig. S2d†). Energy dispersive X-ray spectrometric (EDS) mapping analyses of different samples for NVO-C1, NVO-C2 and NVO-C3 (Fig. S3a–d†) confirm that all the samples display a homogeneous distribution of Na, V and O of the nanowires, with no other elements detected.

More detailed structural information of the NVO samples was collected by transmission electron microscopy (TEM) and high-resolution transmission electron microscopy (HRTEM). For simple NVO nanowires with no CTAB involved in the reaction, they show straight and uniform nanowire morphologies with a diameter of around 200 nm as indicated in Fig. 3a and the inset, without any kinked or hierarchical morphology.

Significantly, Fig. 3b and the inset indicate that NVO-C1 has an obvious kinked nanowire structure, but some stackings and dislocations can be observed, indicating the nonuniformity to some extent. For the TEM image of NVO-C2 shown in Fig. 3c and the inset, the kinked nanowire structure can be obviously observed and the structure is uniform. It can be recognized that the kinked nanowire is composed of many repeated small interconnected nanorods, with a diameter of 200 nm and a length of around 600 nm for every single nanorod. Each two nanorods are connected with each other orientally, and this unit repeats to form the long zigzag nanowire, indicating excellent periodicity. This is a typical interior hierarchical structure.[36,37] For NVO-C3 in Fig. 3d and the inset, the nanowire structure constructed from short nanorods can still be observed, but is ambiguous as the nanorods are stacked with each other with almost no orientation or tendency. The HRTEM images of simple NVO, NVO-C1, NVO-C2 and NVO-C3 are shown in Fig. 3e–h, respectively. All HRTEM images show clear lattice fringes, indicating the high crystallinity of the samples. The addition of CTAB does not influence the crystal structure of the samples. The lattice fringes confirm the pure crystalline phase of the samples. The corresponding selected area electron diffraction (SAED) patterns of the insets in Fig. 3e–h indicate the single crystallinity of NVO. The detailed structures of the junctions for the NVO-C1, NVO-C2 and NVO-C3 hierarchical zigzag nanowires are shown in the HRTEM image of Fig. S4a–c,† respectively. The boundaries between two individual short nanorods can be seen in the HRTEM images, and the Moiré fringes indicate that the two individual nanorods are stacking together. To better understand the crystal orientation of the as-synthesized samples, further evidence of the corresponding SAED patterns for NVO-C1, NVO-C2 and NVO-C3 junctions is shown in Fig. S4d–f,† respectively. Two identical crystal lattices can be observed for NVO-C1, and after determination of the
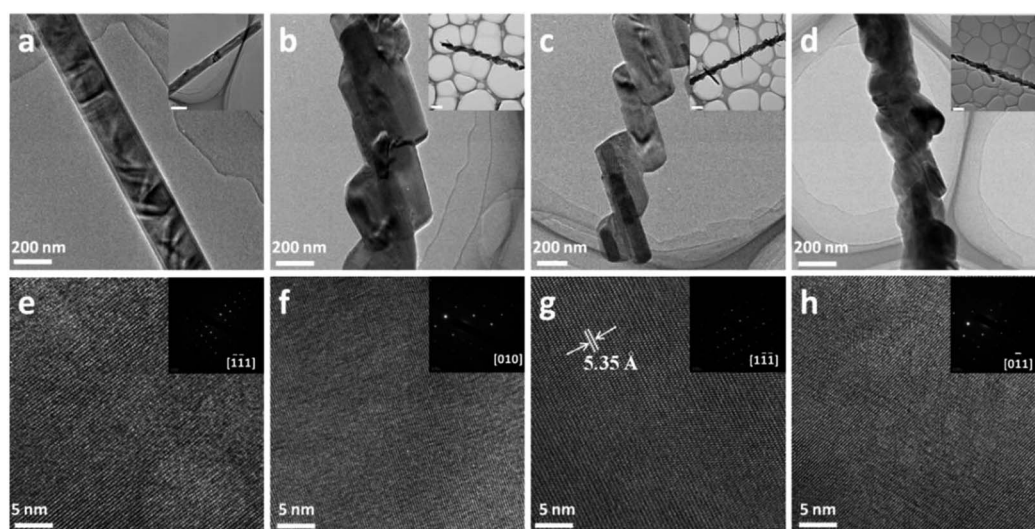

Fig. 3 Morphologies of products synthesized with different amounts of CTAB. TEM images of simple NVO (a), NVO-C1 (b), NVO-C2 (c) and NVO-C3 (d), and the insets in (a–d) show the morphologies in different scales (scale bar for a inset: 200 nm; for b–d insets: 1 μm). HRTEM images of simple NVO (e), NVO-C1 (f), NVO-C2 (g) and NVO-C3 (h), and the corresponding SAED patterns are shown in the insets of (e–h) with zone axis indicated.

This journal is © The Royal Society of Chemistry 2015

Energy Environ. Sci., 2015, 8, 1267–1275 | 1269

crystal lattice we can see that they are sharing the same zone axis, indicating that the two short nanorods have the same crystal orientation. This phenomenon can also be observed in NVO-C2 and NVO-C3, showing that the crystal orientations of the different samples are the same. Therefore, the possible mechanism can be proposed for the formation of hierarchical zigzag nanowires: when NaOH and CTAB are added into $H_2V_3O_8$ nanowires dispersed in ethanol and stirred, $H_2V_3O_8$ and NaOH will closely contact with each other. Meanwhile, CTAB will adhere on the $H_2V_3O_8$ nanowires uniformly because of its property as a cationic surfactant. During the following calcination, the Na ions will diffuse into the $H_2V_3O_8$ nanowires because of the concentration gradient and the principle of minimum energy, and occupy the octahedral and tetrahedral sites afterwards. As the crystal structure of $H_2V_3O_8$ and $Na_{1.25}V_3O_8$ are very similar (both composed of V_3O_8 layers consisting of VO_6 octahedra and VO_5 trigonal bipyramids), there is a definite crystallographic relationship between the precursor and the product, and therefore the topotactic intercalation process will lead to a minimal change in the structure and morphology. Concurrently, the gasification of CTAB will change the surface orientation which will cause the morphology to break into nanorods. Due to the high temperature during annealing, the nanorods will attach with each other because of the self-assembly and oriented attachment process. The spontaneous self-organization of adjacent nanorods which share a common crystallographic orientation is due to the tendency to reduce the overall surface energy.[33,38] The short nanorods link with each other together with specific orientation and form the hierarchical zigzag nanowires.

Nitrogen sorption isotherms were generated to investigate the Brunauer–Emmet–Teller (BET) surface area. The nitrogen adsorption–desorption isotherms of NVO samples with different CTAB addition contents are given in Fig. S5a–d,† respectively. It can be seen that the samples synthesized with CTAB have much higher surface area than simple NVO. The BET surface area for simple NVO is only 7.8 m^2 g^{-1}, while for NVO-C1, NVO-C2 and NVO-C3, the BET surface areas are 35.8, 40.8 and 31.6 m^2 g^{-1}, respectively. The increase in surface area results from the novel hierarchical zigzag nanowire structure of NVO. The NVO-C2 has the largest surface area, and this may be attributed to the moderate amount of CTAB used in the synthesis: when the amount of CTAB is insufficient, the structure cannot be formed effectively and completely; when CATB is excessive, the reaction is too fast and the structure is destroyed, also there can be stacking during the reaction because of the large amount of CTAB. This is in good correspondence with TEM images in Fig. 3. Remarkably, the structure can effectively increase the reaction sites and facilitate the charge transfer and has a great potential in improving the electrochemical properties.

The electrochemical performances of simple NVO, NVO-C1, NVO-C2 and NVO-C3 were characterized by using CR2025 coin cells with sodium metal as the counter electrode. The redox couple properties of the samples are demonstrated by cyclic voltammetric (CV) curves in Fig. 4a for the initial cycle at a scan rate of 0.1 mV s^{-1} in a voltage range of 1.5 to 4.0 V vs. Na^+/Na. It

can be identified that the NVO-C2 has a larger curve area and higher redox peak current than other samples, indicating the highest capacity and the fastest kinetics for Na ion insertion/extraction of NVO-C2. Two oxidation (Na^+ extraction) peaks can be observed near 2.6 and 3.5 V, respectively, with the corresponding reduction (Na^+ insertion) peaks located around 2.3 and 3.3 V accordingly. The NVO-C1, NVO-C3 and simple NVO have oxidation/reduction peak shifts compared to NVO-C2, and the difference between the peaks are increasing in order, which should be attributed to the electrode polarization during cycling because of the lower kinetics. The charge–discharge profiles of simple NVO, NVO-C1, NVO-C2 and NVO-C3 at a current density of 100 mA g^{-1} over a potential window of 1.5 to 4.0 V are presented in Fig. 4b. All the samples exhibit clear charge–discharge voltage plateaus, corresponding well with the oxidation/reduction peaks in the CV curve. The specific discharge capacity of NVO-C2 is 171.9 mA h g^{-1}, significantly higher than those of 154.3 and 126.6 mA h g^{-1} for NVO-C1 and NVO-C3, respectively, and about two times the value of the discharge capacity of simple NVO, which is only 83.5 mA h g^{-1}. The coulombic efficiencies of the samples all exceed 97%, indicating the good reversibility of NVO.

The detailed reaction kinetics of the electrode materials were investigated using electrochemical impedance spectroscopy (EIS) in the frequency range from 100 kHz to 0.01 Hz as shown in Fig. 4c. In the equivalent circuit (inset of Fig. 4c), R_e represents the equivalent series resistance that includes all Ohmic resistance due to the electrolyte and other parts of the cell. CPEs refers to constant phase elements, revealing the non-ideal capacitance due to the surface roughness, while R_{ct} and R_f stand for the charge transfer resistance through the electrode/electrolyte interface and the contacts in between nanowires, respectively. All the Nyquist plots are composed of a semicircle in the high frequency region, combined with a slanted curve in the low-frequency region. The semicircle is ascribed to the Na ion migration through the interface between the surface layer of the electrode and the electrolyte. It can be clearly seen that the charge-transfer resistance R_{ct} of NVO-C2 is the lowest, followed by NVO-C1 and NVO-C3, and simple NVO has the highest R_{ct}. The slanted line is attributed to the diffusion of sodium ions in the bulk of the electrode material, and the diffusion coefficient value (D) of the sodium ions can be calculated using the equation $D = 0.5(RT/AF^2\sigma_wC)^2$, where R is the gas constant, T is the temperature, A is the area of the electrode surface, F is Faraday's constant, σ_w is the Warburg factor, and C is the molar concentration of Na ions.[39] The calculated Na ion diffusion coefficient values for simple NVO, NVO-C1, NVO-C2 and NVO-C3 are 1.6×10^{-13}, 0.8×10^{-12}, 2.2×10^{-12} and 1.0×10^{-12} cm^2 s^{-1}, respectively, indicating the best diffusion ability of Na ions in NVO-C2.

It can be concluded from the above electrochemical analyses that the NVO-C2 has the best electrochemical performance, and this is subsequently verified. Fig. 4d exhibits the cyclic performance of simple NVO, NVO-C1, NVO-C2 and NVO-C3 at a moderate current density of 200 mA g^{-1}. Obviously the NVO-C2 has the highest initial capacity, which is 158.7 mA h g^{-1}, higher than 134.8, 110.7 and 69.3 mA h g^{-1} for NVO-C1, NVO-C3 and

1270 | *Energy Environ. Sci.*, 2015, **8**, 1267–1275

This journal is © The Royal Society of Chemistry 2015
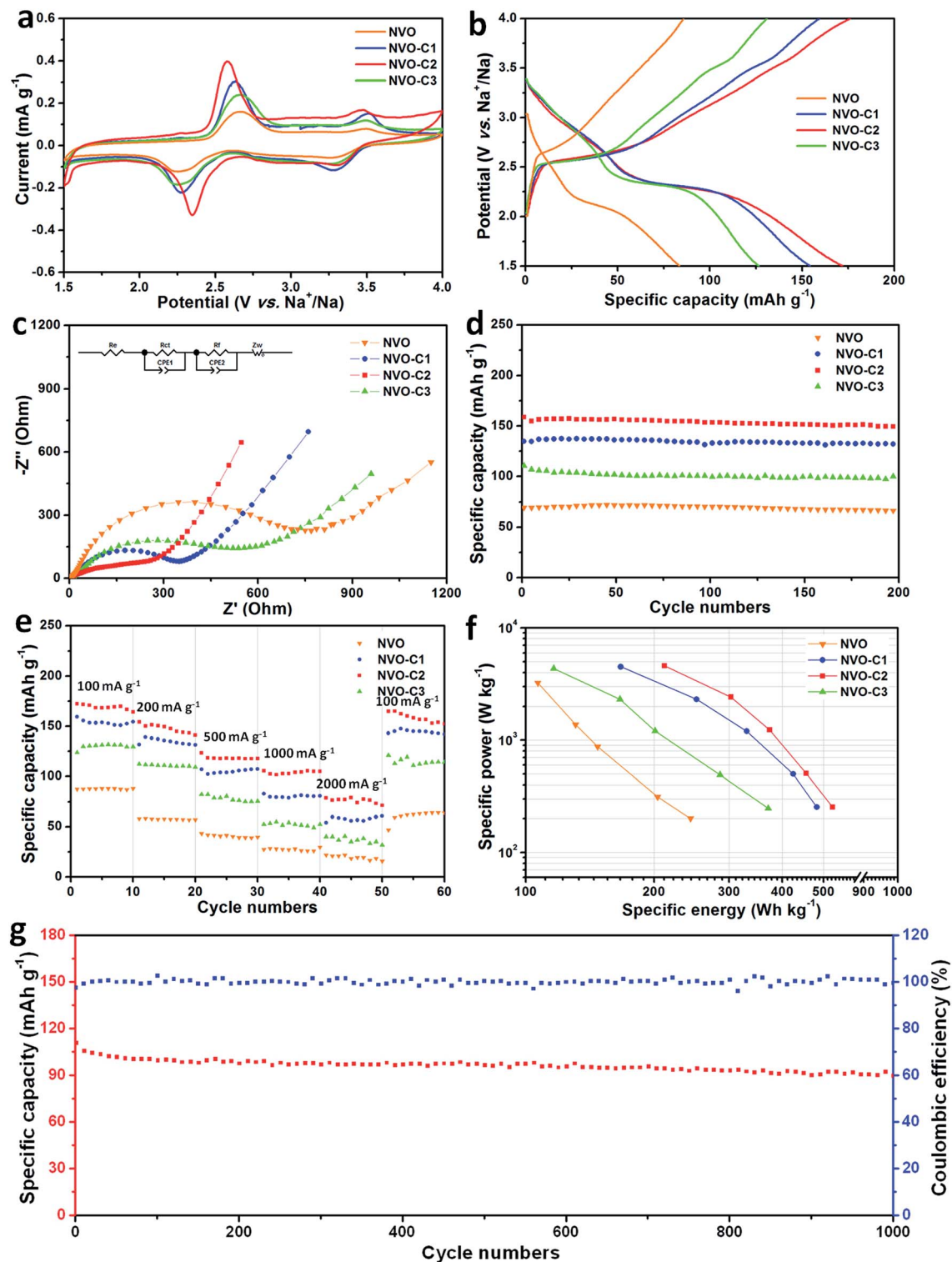
Fig. 4 Electrochemical performances of NVO-C1, NVO-C2, NVO-C3 and simple NVO as the cathode in sodium ion batteries. (a) Cyclic vol-tammograms at a scan rate of 0.1 mV s^{-1} in a voltage range of 1.5–4.0 V; (b) galvanostatic charge–discharge curves of different samples at a current density of 100 mA g^{-1}; (c) alternating-current impedance plots of the samples from 0.01 Hz to 100 kHz; (d) cycling performance of the samples cycled at 200 mA g^{-1} in 1.5–4.0 V for 200 cycles; (e) rate performance at various current rates from 100 mA g^{-1} to 2000 mA g^{-1}; (f) Ragone plots of samples as sodium ion battery cathodes; (g) charge–discharge cycling test of the NVO-C2 nanowire cathode at high current densities of 1000 mA g^{-1} for 1000 cycles.

simple NVO, respectively, corresponding well with the charge–discharge curve in Fig. 4b. All the samples exhibit excellent cycling stability, the capacity retentions are all around 95% after 200 cycles for the samples, indicating the excellent stability due to the topotactic synthetic route of NVO. The cycling stability of NVO compares well with the commercial lithium-ion batteries and exceeds most of the other rechargeable batteries. For further evaluation of the electrochemical behaviour, rate performance at progressively increased current densities (ranging from 100 to 2000 mA g^{-1}) was measured as shown in Fig. 4e. All the samples exhibit a reasonably good cycling response at various current rates. Remarkably, even at a high current density of 2000 mA g^{-1}, the capacity of NVO-C2 can still reach 79.1 mA h g^{-1}, about half of the initial capacity at 100 mA g^{-1} while the current density is 20 times higher. For NVO-C1 and NVO-C3, the capacities at 2000 mA g^{-1} are 56.6 and 36.7 mA h g^{-1}, much lower than that of NVO-C2. For simple NVO, the rate capability is inferior with a capacity of only 15.8 mA h g^{-1} at 2000 mA g^{-1}. The charge–discharge profiles of NVO-C2 at different current densities are shown in Fig. S6.† The plateaus can be clearly distinguished under each current density, and the potential difference is insignificant, indicating good reversible redox reactions during charge–discharge. Even suffering from rapid changes of the current densities, the NVO nanowire electrodes exhibit stable capacity at each current. When the current is turned back to 100 mA g^{-1}, the NVO-C2 is able to maintain a high capacity of 165.0 mA h g^{-1} again, about 95% of the initial capacity at 100 mA g^{-1} before high rate measurement. To our knowledge, this is the best performance of NVO in sodium-ion batteries ever reported, both in cycling stability and rate capability. Also the sodium-ion battery performance of our sample exceeds that of most other sodium-ion battery cathodes,[31,40–42] and is even comparable to the electrode materials used in lithium-ion batteries.[43–45]

The specific energy and specific power of simple NVO, NVO-C1, NVO-C2 and NVO-C3 are shown in the Ragone plot in Fig. 4f. The NVO-C2 exhibits the highest energy density at 100 mA g^{-1}, which is 524.8 W h kg^{-1}. Also it can significantly deliver a power density of about 4700 W kg^{-1}. This shows that our as-synthesized material is a promising candidate for energy storage systems with both high-power and high-energy densities. Fig. 4g displays the long-life performance of the NVO-C2 electrode under a high current density of 1000 mA g^{-1}. The initial specific discharge capacity is 105.9 mA h g^{-1}, and after 500 cycles, the capacity is 97.5 mA h g^{-1}, with a capacity retention of 92.0%; after 1000 cycles, the capacity can still maintain 92.2 mA h g^{-1}, and the capacity retention is 87.0%, corresponding to a capacity fading of 0.0138% per cycle. The coulombic efficiency can reach up to 99% in the overall battery operation, indicating good reversibility. This is the long-life stability of NVO in sodium-ion batteries ever reported, and this optimum performance demonstrates the successful synergistic effect of our sample. It should be noted that the superior performance is achieved without carbon content in the material, which can be proved by the Raman analysis in Fig. S7† that no existence of D or G characteristic peaks of carbon can be observed. The cycling stability after 1000 cycles is better than other sodium-ion battery materials[46–49] and even better than many of the as-reported materials in lithium-ion

batteries.[50–52] The coin-cell type full sodium-ion batteries consisting of the NVO-C2 positive and commercial carbon nanofiber negative electrodes (NVO-C2/CNF full cell) are also fabricated and the electrochemical performances are shown in Fig. S8.† It can be seen in Fig. S8a† that the initial capacity is about 143.8 mA h g^{-1}, followed by 35.0 mA h g^{-1} capacity drop for the second cycle. The relatively fast capacity decrease for the initial cycles should be attributed to the formation of the solid electrolyte interface (SEI) layer at the anode surface and the irreversible sodium absorption onto the CNF, which is a common phenomenon for the carbon-based anode for sodium-ion batteries.[53,54] And a voltage plateau for the NVO-C2/CNF full cell can be observed around 2.3 V. Fig. S8b† is the cycling performance for the NVO-C2/CNF full cell cycled under 100, 200 and 500 mA g^{-1}. It can be seen that after the initial several cycles, the discharge capacity is stabilized. For the performance cycled at 100 mA g^{-1}, after 200 cycles, the capacity is 78.5 mA h g^{-1}, corresponding to the capacity retention of about 82% from the 10th to 100th cycle, and 75% from the 10th to 200th cycle. For 200 mA g^{-1}, the capacity retention from the 10th to 200th cycle is 77%. For 500 mA g^{-1}, the initial capacity is 88.7 mA h g^{-1}, and the capacity retention can reach up to 68% from the 10th to 200th cycle. Taking the limitations caused by the quality of the commercial carbon nanofiber anode, the suitability of the electrolyte system for both the electrodes, and other factors into consideration, the Na-ion full cell performance can be further improved if a more suitable sodium-ion anode is developed. The excellent cycling stability should be attributed to the good Na ion insertion/deinsertion reversibility during cycling. To verify this, we further investigate the electrochemical Na ion insertion/extraction process via in situ XRD for the NVO-C2 sample as shown in Fig. S9.† The as-prepared NVO-C2 in situ cell was discharged to 1.5 V and then charged to 4.0 V using a constant current of 100 mA g^{-1} at 25 °C and was never removed from the diffractometer. The peak evolution can be clearly observed, indicating the typical intercalation mechanism as well as structure change during charge–discharge. The initial XRD pattern is the same as the XRD pattern at the very end, indicating the good reversibility of the crystal structure. For the characteristic peaks at different charge–discharge states, a peak shift to left during discharge and followed by a shift to right during charge can be clearly observed, which is due to the fact that during discharge Na ions are intercalated into the layers and cause the layer expansion (shift to lower angle), and when the Na ions are deintercalated during charge, the layers shrink and the peaks shift to a higher angle. The in situ XRD diffraction pattern clearly proves the good reversibility and the intercalation mechanism of the NVO. However, as the Na ions located in the tetrahedral sites are hard to characterize during charge–discharge, the accurate phases for charge–discharge plateaus are difficult to define. Nevertheless we can tell undoubtedly that the layered structure is well maintained during the charge–discharge process.

Discussion

This superior performance should be attributed to the unique morphology and the optimized crystal structure. First, the hierarchical structure provides much larger surface area of the

nanowires as shown in the BET measurements, which facilitates electrochemical reactions and ensures efficient penetration of the electrolyte into the active materials, endowing the hierarchical NVO nanowires with a reduced Na ion diffusion length, thus resulting in improved electrochemical kinetics. Also the hierarchical zigzag structure can effectively alleviate the self-aggregation and volume change during cycling. For simple nanowires, after several cycles the nanowires are easy to stack together, which decreases the effective electrolyte–electrode contact area and limits ion diffusion. And the volume change is severe for the simple nanowire structure during ion insertion/deinsertion, resulting in structural degradation. The hierarchical zigzag structure creates more space and voids between the nanowires. During cycling, the interconnected voids can effectively buffer self-aggregation, providing consistent ion pathways and reaction sites. Moreover, the hierarchical structure is more robust because of the junctions which can release the stress and strain. Therefore the morphology can be well maintained after charge–discharge for many cycles, without hampering the electrochemical performance. This can be verified in Fig. S10,† which shows the morphologies of simple NVO and hierarchical NVO-C2 nanowires after 100 cycles under a current density of 100 mA g^{-1}. The NVO-C2 maintains the hierarchical nanowire morphology very well, while for the simple NVO nanowire, the structure is completely damaged. It can also be testified from the difference of cycling performances under high current densities for simple NVO and hierarchical zigzag NVO nanowires. Fig. S11† shows the cycling performance of simple NVO under 1000 mA g^{-1} current density, and the capacity fades from 54.9 mA h g^{-1} in the initial cycle to only 23.6 mA h g^{-1} after 80 cycles, much worse than that of NVO-C2.

In addition, the topotactic synthesis also contributes to the improved performance. Using the topotactic synthesis route, the crystal structure change between the precursor and the final product can be minimized. Here, there are definite crystallographic relationships between the $H_2V_3O_8$ and $Na_{1.25}V_3O_8$, whose crystal structures are both made up of V_3O_8 layers consisting of VO_6 octahedra and VO_5 distorted trigonal bipyramids interconnected with each other. Due to the similar crystal structure, during synthesis the structure change is minimal and the defects, aggregates and ruptures during synthesis can be avoided to the uttermost, and the crystallinity of the electrode material is also much better. Compared with our uniform and ultralong topotactically synthesized $Na_{1.25}V_3O_8$ using the $H_2V_3O_8$ precursor in our experiment, the $Na_{1.25}V_3O_8$ nanowires in other reports where V_2O_5 or other vanadium sources were used as the precursor that always contains ruptured short segments and cleavages, and the length is also significantly shorter. To verify the advantage using the topotactic method consistently, we performed a comparison experiment where we used V_2O_5 nanowires as the precursor (SEM image shown in Fig. S12a†) to synthesize $Na_{1.25}V_3O_8$ nanowires in the same experimental parameter. The XRD patterns (Fig. S12b†) indicate that the sample prepared by the V_2O_5 precursor is $Na_{1.25}V_3O_8$ with a monoclinic structure, the same as the $Na_{1.25}V_3O_8$ prepared by $H_2V_3O_8$. But the SEM image shows that the nanowires are not uniform and the surface is not smooth, also there

are some ruptured short segments that exist as shown in Fig. S12c.† Compared with the precursor V_2O_5 nanowires, the $Na_{1.25}V_3O_8$ cannot maintain the nanowire structure well, which should be attributed to the structure change during the Na ion diffusion process during calcination. We also tested the electrochemical performance of the $Na_{1.25}V_3O_8$ nanowires prepared from V_2O_5, and the behaviour is much worse than that of the $Na_{1.25}V_3O_8$ nanowires prepared by topotactic intercalation: under a current density of 200 mA g^{-1}, the initial discharge capacity is only 49.2 mA h g^{-1}, even lower than that of 69.3 mA h g^{-1} for simple NVO. And the capacity retention of non-topotactically synthesized NVO is also inferior, which is only 73.2% compared with 98.3% of topotactically synthesized simple NVO after 100 cycles (Fig. S12d†). This indicates that the topotactically synthesized $Na_{1.25}V_3O_8$ nanowires with fairly good structural integrity endows the better ionic transport and electron conductivity, resulting in excellent electrochemical performance.

Conclusions

We fabricated novel hierarchical $Na_{1.25}V_3O_8$ nanowires *via* a topotactically synthetic method. The monoclinic $Na_{1.25}V_3O_8$ nanowires consist of small nanorods linked repeatedly and have a uniform zigzag shape, exhibiting excellent performance of high capacity (158.7 mA h g^{-1} at 200 mA g^{-1}), cycling stability (capacity fading of 0.0138% per cycle at 1 A g^{-1} for 1000 cycles) as well as rate capability (79.1 mA h g^{-1} at 2 A g^{-1}) as sodium-ion battery cathodes, which is among the best performance for all the reported cathode materials for sodium-ion batteries. This demonstrates the successful synergistic effect between the crystal structure modification and morphology optimization. We believe that the rational synthetic strategy presented here can provide new thoughts for fabricating electrode materials in energy storage devices, and the cathode materials that we synthesized with high specific energy and power will speed up the exploration and development of sodium-ion batteries as well as other next-generation rechargeable batteries for the application in large scale energy storage and utility.

Experimental section

Synthesis

For a typical synthesis, V_2O_5, H_2O_2, NaOH, polyethylene glycol (PEG) and cetyltrimethyl ammonium bromide (CTAB) were analytical grade reagents, purchased from Sinopharm Chemical Reagent Co. Ltd., Shanghai, China. All chemicals were used as received without further treatment. The $H_2V_3O_8$ nanowires were prepared in two steps by the modified method of our previous work.[35] First, 1.3 mmol V_2O_5 (0.237 g) and 0.04 g PEG-10K were added slowly in 15 mL 30% H_2O_2. The as-obtained orange solution was mixed thoroughly and stirred continuously, then transferred into a Teflon-lined stainless steel autoclave and kept at 180 °C for 2 days. The products were collected and washed with deionized water and ethanol repeatedly, and finally dried at 70 °C in air to obtain the ultralong $H_2V_3O_8$ nanowire bundles.

This journal is © The Royal Society of Chemistry 2015

Energy Environ. Sci., 2015, **8**, 1267–1275 | **1273**

To obtain the $Na_{1.25}V_3O_8$, first, $H_2V_3O_8$ nanowires were dispersed in 20 mL ethanol and stirred for 10 min, and then NaOH with 1 : 1.3 m/m ratio was added into the dispersed solution and stirred. Then, CTAB (0.1 g) was added into the mixed solution and stirred for another 30 min. Then the solution was kept in a water bath at 70 °C for 5 h and then dried at 70 °C for 12 h to allow alcohol evaporation. Finally the solid was annealed at 450 °C for 5 h in air with a temperature ramping rate of 10 °C min^{-1} and cooled down to room temperature to obtain a red brown powder. For comparison, different masses of CTAB (0, 0.05, 0.2 g) were used while all other procedures remain the same.

Characterization

X-ray diffraction (XRD) measurements were performed to investigate the crystallographic information using a Bruker D8 Advance X-ray diffractometer with a non-monochromated Cu Kα X-ray source. Scanning electron microscopy (SEM) images and energy dispersive X-ray spectra (EDS) were collected with a JEOL JSM-7100F SEM/EDS microscope at an acceleration voltage of 15 kV. Transmission electron microscopy (TEM) and high resolution transmission electron microscopy (HRTEM) images were recorded with a JEOL JEM-2100F STEM/EDS microscope. Brurauer–Emmerr–Teller surface area was measured using a Tristar II 3020 instrument by adsorption of nitrogen at 77 K. Raman spectra were acquired using a Renishaw RM-1000 laser Raman microscopy system.

Electrochemical measurements

The electrochemical properties were measured with 2025 coin cells assembled in a glove box filled with pure argon gas. In sodium half cells, sodium metal was used as the anode, a 1 M solution of $NaClO_4$ in ethylene carbon (EC)–dimethyl carbonate (DMC) (1 : 2 w/w) was used as the electrolyte, and a Whatman Glass Microfibre Filter (Grade GF/F) was used as the separator. The cathode electrodes were produced with a 70% NVO active material, 20% carbon black and 10% poly(tetrafluoroethylene), and the active material content in the electrode was around 3.0 mg. The NVO/CNF full cell was fabricated using as-synthesized NVO as the cathode, a commercial carbon nanofiber (Sigma-Aldrich Co.) as the anode and was cathode-limited with the same separator and electrolyte as half-cell. Galvanostatic charge–discharge measurement was performed in the potential range of 1.5 to 4.0 V *vs.* Na$^+$/Na with a multi-channel battery testing system (LAND CT2001A). Cyclic voltammetry curves (CV) and electrochemical impedance spectra (EIS) were recorded with an electrochemical workstation (Autolab PGSTAT 302 and CHI 760D). The $Na_{1.25}V_3O_8$/Na cell for *in situ* XRD measurements was assembled in a glovebox filled with Ar, and then galvanostatic charge–discharge cycling was studied in a potential range of 1.5–4.0 V *versus* Na$^+$/Na with the multichannel battery testing system. The sample was placed right behind an X-ray-transparent beryllium window, which also acts as a current collector. The *in situ* XRD patterns were collected, using a Bruker D8 Discover Diffractometer with Cu-Kα radiation over the 2θ range (11–31°) in a still mode with each data acquisition

taking 3 min. The specific energy E (W h kg^{-1}) can be calculated by $E = \int_0^t \frac{I_o}{m} V(t) dt$, where t is the discharge time, I_o (A) is the constant current, m (kg) is the mass of the active material, and $V(t)$ is the time-dependent voltage in the dimension of V. The specific power P (W kg^{-1}) can be calculated by $P = E/t$.

Acknowledgements

Notes and references

1 S. Chu and A. Majumdar, *Nature*, 2012, **488**, 294–303.
2 N. Armaroli and V. Balzani, *Angew. Chem., Int. Ed.*, 2007, **46**, 52–66.
3 Y. Gogotsi and P. Simon, *Science*, 2011, **334**, 917–918.
4 J. Liu, *Adv. Funct. Mater.*, 2013, **23**, 924–928.
5 G. L. Soloveichik, *Annu. Rev. Chem. Biomol. Eng.*, 2011, **2**, 503–527.
6 M. M. Thackeray, C. Wolverton and E. D. Isaacs, *Energy Environ. Sci.*, 2012, **5**, 7854–7863.
7 T. H. Kim, J. S. Park, S. K. Chang, S. Choi, J. H. Ryu and H. K. Song, *Adv. Energy Mater.*, 2012, **2**, 860–872.
8 M. S. Whittingham, *Chem. Rev.*, 2004, **104**, 4271–4302.
9 B. Dunn, H. Kamath and J.-M. Tarascon, *Science*, 2011, **334**, 928–935.
10 M. Armand and J.-M. Tarascon, *Nature*, 2008, **451**, 652–657.
11 J. B. Goodenough and K.-S. Park, *J. Am. Chem. Soc.*, 2013, **135**, 1167–1176.
12 J.-M. Tarascon and M. Armand, *Nature*, 2001, **414**, 359–367.
13 M. H. Hana, E. Gonzaloa, G. Singha and T. Rojo, *Energy Environ. Sci.*, 2015, **8**, 81–102.
14 H. Zhou, *Energy Environ. Sci.*, 2013, **6**, 2256.
15 V. Palomares, M. Casas-Cabanas, E. Castillo-Martínez, M. H. Han and T. Rojo, *Energy Environ. Sci.*, 2013, **6**, 2312–2337.
16 M. D. Slater, D. Kim, E. Lee and C. S. Johnson, *Adv. Funct. Mater.*, 2013, **23**, 947–958.
17 S. P. Ong, V. L. Chevrier, G. Hautier, A. Jain, C. Moore, S. Kim, X. Ma and G. Ceder, *Energy Environ. Sci.*, 2011, **4**, 3680–3688.
18 S. W. Kim, D. H. Seo, X. Ma, G. Ceder and K. Kang, *Adv. Energy Mater.*, 2012, **2**, 710–721.

1274 | *Energy Environ. Sci.*, 2015, **8**, 1267–1275

This journal is © The Royal Society of Chemistry 2015

19 V. Palomares, P. Serras, I. Villaluenga, K. B. Hueso, J. Carretero-González and T. Rojo, *Energy Environ. Sci.*, 2012, **5**, 5884–5901.

20 D. Nguyen, J. Gim, V. Mathew, J. Song, S. Kim, D. Ahn and J. Kim, *ECS Electrochem. Lett.*, 2014, **3**, A69–A71.

21 S. Hartung, N. Bucher, V. S. Nair, C. Y. Ling, Y. Wang, H. E. Hoster and M. Srinivasan, *ChemPhysChem*, 2014, **15**, 2121–2128.

22 H. He, G. Jin, H. Wang, X. Huang, Z. Chen, D. Sun and Y. Tang, *J. Mater. Chem. A*, 2014, **2**, 3563–3570.

23 S. Liang, T. Chen, A. Pan, D. Liu, Q. Zhu and G. Cao, *ACS Appl. Mater. Interfaces*, 2013, **5**, 11913–11917.

24 H. Wang, S. Liu, Y. Ren, W. Wang and A. Tang, *Energy Environ. Sci.*, 2012, **5**, 6173–6179.

25 H. Wang, W. Wang, Y. Ren, K. Huang and S. Liu, *J. Power Sources*, 2012, **199**, 263–269.

26 Y. Tang, D. Sun, H. Wang, X. Huang, H. Zhang, S. Liu and Y. Liu, *RSC Adv.*, 2014, **4**, 8328–8334.

27 H. He, X. Zeng, H. Wang, N. Chen, D. Sun, Y. Tang, X. Huang and Y. Pan, *J. Electrochem. Soc.*, 2015, **162**, A39–A43.

28 L. Mai, X. Tian, X. Xu, L. Chang and L. Xu, *Chem. Rev.*, 2014, **114**, 11828–11862.

29 P. Yang and J.-M. Tarascon, *Nat. Mater.*, 2012, **11**, 560–563.

30 A. S. Aricò, P. Bruce, B. Scrosati, J.-M. Tarascon and W. Van Schalkwijk, *Nat. Mater.*, 2005, **4**, 366–377.

31 S. Li, Y. Dong, L. Xu, X. Xu, L. He and L. Mai, *Adv. Mater.*, 2014, **26**, 3545–3553.

32 L. Mai, Q. Wei, Q. An, X. Tian, Y. Zhao, X. Xu, L. Xu, L. Chang and Q. Zhang, *Adv. Mater.*, 2013, **25**, 2969–2973.

33 L. Mai, F. Yang, Y. Zhao, X. Xu, L. Xu and Y. Luo, *Nat. Commun.*, 2011, **2**, 381.

34 X. Xu, Y. Luo, L. Mai, Y. Zhao, Q. An, L. Xu, F. Hu, L. Zhang and Q. Zhang, *NPG Asia Mater.*, 2012, **4**, e20.

35 Q. An, J. Sheng, X. Xu, Q. Wei, Y. Zhu, C. Han, C. Niu and L. Mai, *New J. Chem.*, 2014, **38**, 2075–2080.

36 S. Li, Y. Dong, D. Wang, W. Chen, L. Huang, C. Shi and L. Mai, *Front. Phys.*, 2014, **9**, 303–322.

37 L. Xu, Z. Jiang, Q. Qing, L. Mai, Q. Zhang and C. M. Lieber, *Nano Lett.*, 2013, **13**, 746–751.

38 M. Niederberger and H. Cölfen, *Phys. Chem. Chem. Phys.*, 2006, **8**, 3271–3287.

39 L. Mai, S. Li, Y. Dong, Y. Zhao, Y. Luo and H. Xu, *Nanoscale*, 2013, **5**, 4864–4869.

40 V. Raju, J. Rains, C. Gates, W. Luo, X. Wang, W. F. Stickle, G. D. Stucky and X. Ji, *Nano Lett.*, 2014, **14**, 4119–4124.

41 D. Buchholz, A. Moretti, R. Kloepsch, S. Nowak, V. Siozios, M. Winter and S. Passerini, *Chem. Mater.*, 2013, **25**, 142–148.

42 I. Hasa, J. Hassoun, Y. K. Sun and B. Scrosati, *ChemPhysChem*, 2014, **15**, 2152–2155.

43 H. Liu and W. Yang, *Energy Environ. Sci.*, 2011, **4**, 4000–4008.

44 S. Jeong, S. Park and J. Cho, *Adv. Energy Mater.*, 2011, **1**, 368–372.

45 Y. Dong, S. Li, H. Xu, M. Yan, X. Xu, X. Tian, Q. Liu and L. Mai, *Phys. Chem. Chem. Phys.*, 2013, **15**, 17165–17170.

46 C. Zhu, K. Song, P. A. van Aken, J. Maier and Y. Yu, *Nano Lett.*, 2014, **14**, 2175–2180.

47 Y. Cao, L. Xiao, W. Wang, D. Choi, Z. Nie, J. Yu, L. V. Saraf, Z. Yang and J. Liu, *Adv. Mater.*, 2011, **23**, 3155–3160.

48 S. Y. Lim, H. Kim, J. Chung, J. H. Lee, B. G. Kim, J.-J. Choi, K. Y. Chung, W. Cho, S.-J. Kim and W. A. Goddard, *Proc. Natl. Acad. Sci. U. S. A.*, 2014, **111**, 599–604.

49 S.-M. Oh, S.-T. Myung, J.-Y. Hwang, B. Scrosati, K. Amine and Y.-K. Sun, *Chem. Mater.*, 2014, **26**, 6165–6171.

50 Q. Wei, Q. An, D. Chen, L. Mai, S. Chen, Y. Zhao, K. M. Hercule, L. Xu, A. Minhas-Khan and Q. Zhang, *Nano Lett.*, 2014, **14**, 1042–1048.

51 X. Zhang, F. Cheng, J. Yang and J. Chen, *Nano Lett.*, 2013, **13**, 2822–2825.

52 Y. Zhao, L. Peng, B. Liu and G. Yu, *Nano Lett.*, 2014, **14**, 2849–2853.

53 S. Komaba, W. Murata, T. Ishikawa, N. Yabuuchi, T. Ozeki, T. Nakayama, A. Ogata, K. Gotoh and K. Fujiwara, *Adv. Funct. Mater.*, 2011, **21**, 3859–3867.

54 Z. Wang, L. Qie, L. Yuan, W. Zhang, X. Hu and Y. Huang, *Carbon*, 2013, **55**, 328–334.

This journal is © The Royal Society of Chemistry 2015

Energy Environ. Sci., 2015, **8**, 1267–1275 | **1275**